Quantitative structure determination of adsorbed formate and surface hydroxyls on Fe_3O_4(001)

P. T. P. Ryan[1,2], D. J. Payne[2], T. –L. Lee[1], D. A. Duncan[1]*

[1] Diamond Light Source, Harwell Science and Innovation Campus, Didcot, OX11 0QX, UK.
[2] Department of Materials, Imperial College London, SW7 2AZ, UK.

Supplementary information

§1 Normal incidence X-ray standing waves (NIXSW)

The NIXSW technique[1] exploits the creation of an X-ray standing wave (XSW) by the interference between the incident and reflected photon beams when the Bragg condition is satisfied for a crystal. The XSW extends into and out of the bulk of the crystal and has a periodicity equal to the real space distance, d_{hkl}, that corresponds to the interplanar spacing between the Bragg diffraction planes[2] of the selected reflection. By using dynamical diffraction theory to determine the amplitude of the XSW, it can be found that scanning the incident photon energy across the Bragg condition causes the phase of the XSW relative to the Bragg diffraction planes to change by π.[3] As such, while scanning the incident photon energy, the X-ray intensity experienced by a selected emitter, and thus the X-ray absorption yield or photoelectron yield from a selected emitter, will be characteristic of the emitter's location relative to the Bragg diffraction planes of the reflection. These photoelectron yield profiles can be modelled and fitted using dynamical diffraction theory:[1]

$$I = 1 + R\frac{(1+Q)}{(1-Q)} + 2f^{hkl}\sqrt{R}\sqrt{\frac{(1+Q)}{(1-Q)}}\cos(\varphi - 2\pi P^{hkl}). \quad (1)$$

Both R and φ (the reflectivity and phase of the standing wave respectively) can be calculated from the known bulk structure and the measured reflection intensity. Q takes into account the angular dependence of the photoemission intensity and is calculated from tabulated values of the photoemission dipole and higher order asymmetry parameters. Thus, this model equation yields two fitting parameters; the coherent fraction, f^{hkl}, and the coherent position, P^{hkl}.[1] The latter parameter can be interpreted as the position the emitter takes between the Bragg diffraction planes of the

chosen reflection, taking values in the range 0-1 representing the fractional height of the emitter between the Bragg diffraction planes. The former can be loosely interpreted as an order parameter of the emitter around this position in the direction of the reflection, taking values between 0-1 with 1 representing complete order and 0 representing complete disorder.

The application of Fourier analysis to the NIXSW technique allows for the imaging of the real space locations of the selected emitters projected into the primitive unit cell of the substrate in a model free manner (as opposed to the trial and error methodology for the analysis of both SXRD and PhD). With such an analysis, the fitting parameters f^{hkl} and P^{hkl} can more formally be described as the magnitude and phase of the H_{th} order Fourier component, F_H, of the structure factor for the selected emitter, F. In turn, by measuring the photoelectron yield from a number of symmetrically inequivalent reflections, the real space atomic density, $\rho(xyz)$, of the selected emitter can be determined as such:

$$\rho(xyz) \propto \sum f^{hkl} \cos\left(2\pi\left(P^{hkl} - [hx + ky + lz]\right)\right). \quad (2)$$

The (004), (044), (113), $(\bar{1}13)$, (131) and $(\bar{3}11)$ reflections were measured which, after taking into account the symmetry of the inverse spinel Fe_3O_4, provides 17 reflections or sets of Fourier components for equation 1.

§2 Energy scanned photoelectron diffraction (PhD)

PhD[5] exploits the inference of the directly emitted photoelectron wave-field from the core-level of a selected surface emitter with that of the same wave-field backscattered from neighbouring atoms. By scanning the incident photon energy and thus the wavelength of the photoelectron, the directly emitted and backscattered components of the wave-field will come into and out of phase with one and other, producing core-level intensity modulations as a function of photoelectron kinetic energy that are indicative of the local structure of the emitter. PhD spectra were measured for the O 1s core-level region. As with the SXPS and NIXSW measurements, each feature in the O 1s XP spectra were fitted with Voigt functions. To model the variations in intensity due to Auger decay spectra and other secondary electron features in the kinetic energy background, a background template was created by also measuring an extended tail section at higher binding energies than the core-level at each photon energy. The resulting modulations in photoemission intensity from each of the O 1s core-level peaks, $I(E)$, were then used to define a stiff spline, $I_0(E)$, representing the non-diffractive variations in photoelectron intensity (e.g. varying cross-section). The PhD spectra, χ_{exp}, were then calculated by:

$$\chi_{exp} = \frac{I(E) - I_0(E)}{I_0(E)}. \quad (3)$$

Multiple scattering of the backscattered photoelectrons renders it impossible to directly retrieve quantitative structural information from the modulations in χ_{exp}. As such, a trial an error approach is utilised by calculating, using multiple scattering theory, the spectra for a given structure, χ_{theory},comparing that to the experimentally determined χ_{exp} and iterating this process until reasonable agreement between the two is reached. Thus, the technique, like SXRD (but unlike NIXSW), is model dependent. Calculations of χ_{theory} were undertaken using codes developed by Fritzsche.[6–8]

The level of agreement between the calculated and measured spectra for each optimisation iteration was quantified using a reliability factor (R factor):[9]

$$R_{factor} = \frac{\sum\left(\chi_{exp} - \chi_{theory}\right)^2}{\sum \chi_{exp}^2 + \chi_{theory}^2}, \quad (4)$$

An R factor of 0 corresponds to perfect agreement, a value of 1 corresponds to uncorrelated data and a value of 2 corresponds to anti-correlated data. Whilst the lowest achievable R factors are normally found in the range 0.2-0.4, the best achievable R factor is heavily dependent on the quality of the data and the complexity of the system under study. Optimisation of the test structures was undertaken using a particle swarm optimisation (PSO) global search algorithm.[10] In order to calculate the associated uncertainties in the determined structural parameters, a variance in R factor (var(R_{min})) was determined as described by Booth et. al.[11]. Using this variance, the uncertainty in a variable was calculated by varying that parameter until the R factor exceeded the sum of the minimum found R factor and this variance. By this method, the difference between the value of the parameter when it exceeds the variance and at the minimum found R factor is defined as that parameter's uncertainty at one standard deviation.

The optimisation calculations were performed by considering the carboxylate O atoms (O_{HCOO}) and hydroxyl O atoms (O_{OH}) data to consist of a single χ_{exp} dataset. Two distinct bidentate sites were considered for the formate molecule: with the carbon coincident in the $[110]$ direction with either the 1st subsurface Fe_{tet} (*tet*) or an Fe_{tet} interstitial site (*int*) (see Figure 1 in the main article). A bulk terminated substrate was utilised for all calculations present in the main article. For this substrate there are two distinct sites for the O_{OH} atom: *tet* and *int* (see Figure 1 in the main article). Other substrate terminations, i.e. the SCV reconstruction and a one vacancy substrate, are considered and discussed here in the ESI §7,8. Relaxation of the substrate atoms and a comparison between the substrates are outlined below in §9.

Thus, four different combinations of O_{HCOO} and O_{OH} site were considered. For each of the O_{HCOO} and O_{OH} species, data from 9 different photoelectron emission geometries were considered in the structural optimisations. Specifically: 5 beams measured in the [110] crystallographic direction and 4 measured in the [100] crystallographic direction. Note that, PhD is generally insensitive to intramolecular distances in organic molecules due to the weak scattering by low mass atoms and scattering from atoms that lie between the emitter and the detector. Therefore, although the carboxylate carbon atom was present in the modelling, the PhD measurements were insensitive to its position. Hydrogen atoms were not included in the calculation as its scattering cross-section is negligible.

§3 Synchrotron X-ray photoelectron spectroscopy

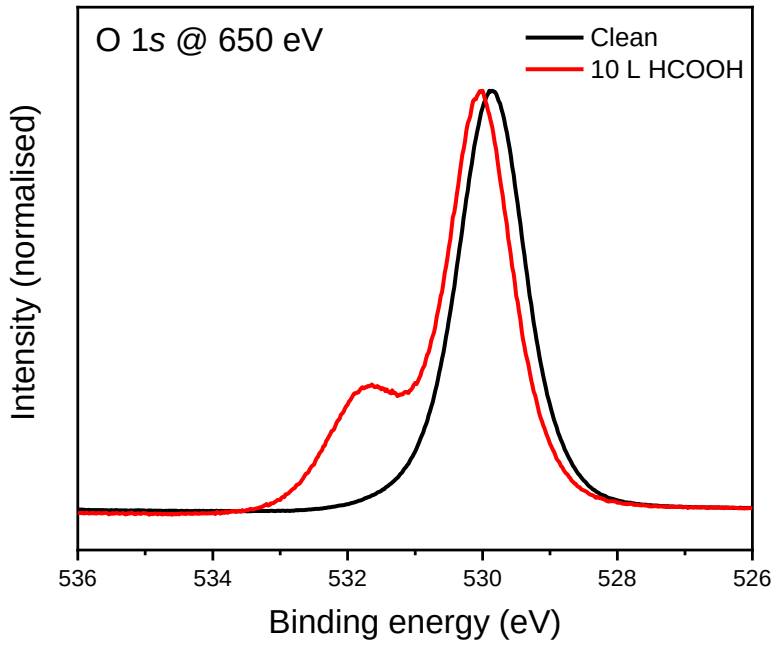

Figure S1 – Shown are the O 1*s* soft X-ray photoelectron spectroscopy (SXPS) spectra for the as prepared clean Fe_3O_4(001) surface and the surface after exposure to 10 L of formic acid. A peak fit of the spectrum for the 10 L formic acid dose is given in the main article.

§4 NIXSW measurements from $(\mathbf{044})$, $(\mathbf{113})$, $(\bar{\mathbf{1}}\mathbf{13})$, $(\mathbf{311})$ and $(\bar{\mathbf{3}}\mathbf{11})$ reflections

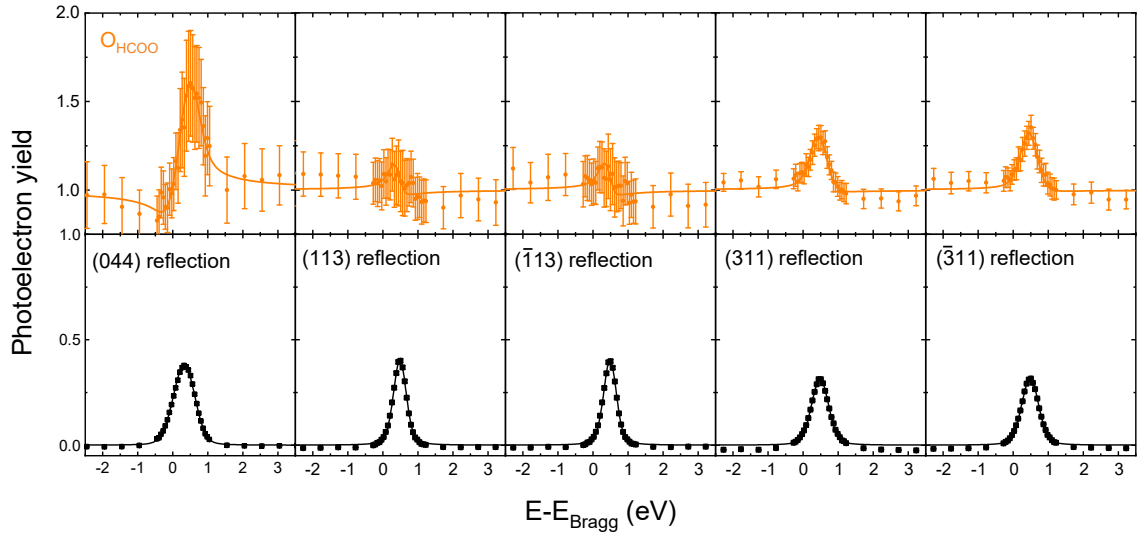

Figure S2 – (044), (113), $(\bar{1}13)$, (311) and $(\bar{3}11)$absorption profiles and reflections for the O_{HCOO} species.

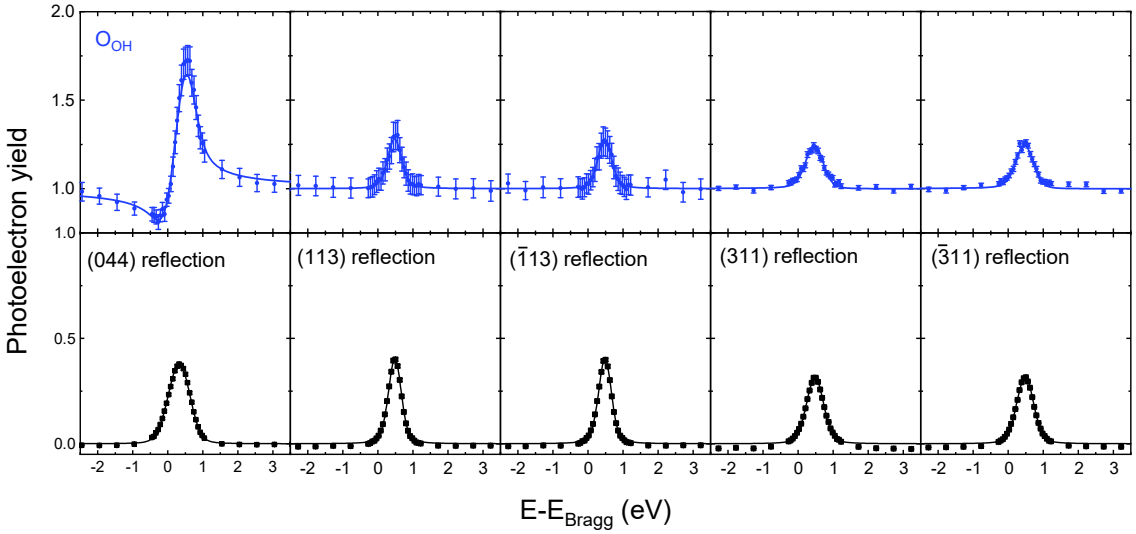

Figure S3 - (044), (113), $(\bar{1}13)$, (311) and $(\bar{3}11)$ absorption profiles and reflections for the O_{OH} species.

Table S1 – The resulting coherent fractions, f^{hkl}, and position, P^{hkl}, from fitting the (044), (113), $(\bar{1}13)$, (311) and $(\bar{3}11)$ measurements for the O_{HCOO}, O_{OH} and C_{exp} (experiment) species. Also given are the theoretical f^{004} and P^{004} for a carbon atom in the *tet*, C_{tet}, and *int*, C_{int}, positions. The values in brackets are the uncertainty in the last significant figure.

	O_{HCOO}	O_{OH}	C_{exp}	C_{tet}	C_{int}
f^{044}	0.59(3)	0.62(4)	0.76(8)	1	1
p^{044}	0.97(1)	0.98(2)	0.75(4)	0.75	0.75
f^{113}	0.34(4)	0.09(1)	0.39(7)	0.70	0.70
p^{113}	0.89(3)	0.97(2)	0.05(4)	0.21	0.96
$f^{\bar{1}13}$	0.32(4)	0.10(2)	0.32(8)	0.70	0.70
$p^{\bar{1}13}$	0.63(3)	0.68(2)	0.80(5)	0.96	0.71
f^{311}	0.11(4)	0.17(2)	0.52(7)	0.70	0.70
p^{311}	0.80(5)	0.88(2)	0.88(4)	0.82	0.07
$f^{\bar{3}11}$	0.05(4)	0.12(2)	0.48(7)	0.70	0.70
$p^{\bar{3}11}$	0.52(8)	0.63(2)	0.63(4)	0.57	0.82

§5 Fitting of carbon real space unit cell densities

To determine the percentage occupation of the two possible bidentate adsorption sites on the $Fe_3O_4(001)$ surface for the formate molecule, mixtures theoretical unit cell densities of the C_{HCOO} atom in the *tet* and *int* sites were fitted to the measured real space density for the C_{HCOO} species. The theoretical unit cell densities for the *tet* and *int* sites were determined by first calculating their corresponding f^{hkl} and P^{hkl} values. For such calculations, the C_{HCOO} atom was placed at the experimentally determined (004) height above the $Fe_3O_4(001)$ surface and all possible positions within the unit cell were determined by taking into account the complete symmetry of the $Fe_3O_4(001)$ unit cell. The resulting coherent fractions were reduced by 0.1 to take into account inherent atomic vibrations that were not modelled directly during the calculation. The complete set of f^{hkl} and P^{hkl} for the two theoretical positions and for the measured C_{HCOO} species are shown in Table S1. The theoretical unit cell densities were then calculated in the exact same manner as was done for the experimental real space imaging which is described in detail in the main article.

The resulting theoretical density map, at the experimentally determined (004) adsorption height, are shown for the *tet* (Figure S5c) and *int* (Figure S5d). The measured density map for C_{HCOO} is shown in Figure S5a, and the resulting best fit with a combination of 63 ± 5% *tet* and 37 ± 5% *int* site occupancy is shown in Figure S5b, again taken at the measured (004) height above the surface. For the fitting, all unit cell densities were normalised to their maximum values. Errors in the percentage occupations were determined by undertaking the same fittings of the unit cell densities but with all the experimental f^{hkl} and P^{hkl} errors either added or subtracted from their experimentally fitted f^{hkl} and P^{hkl} values.

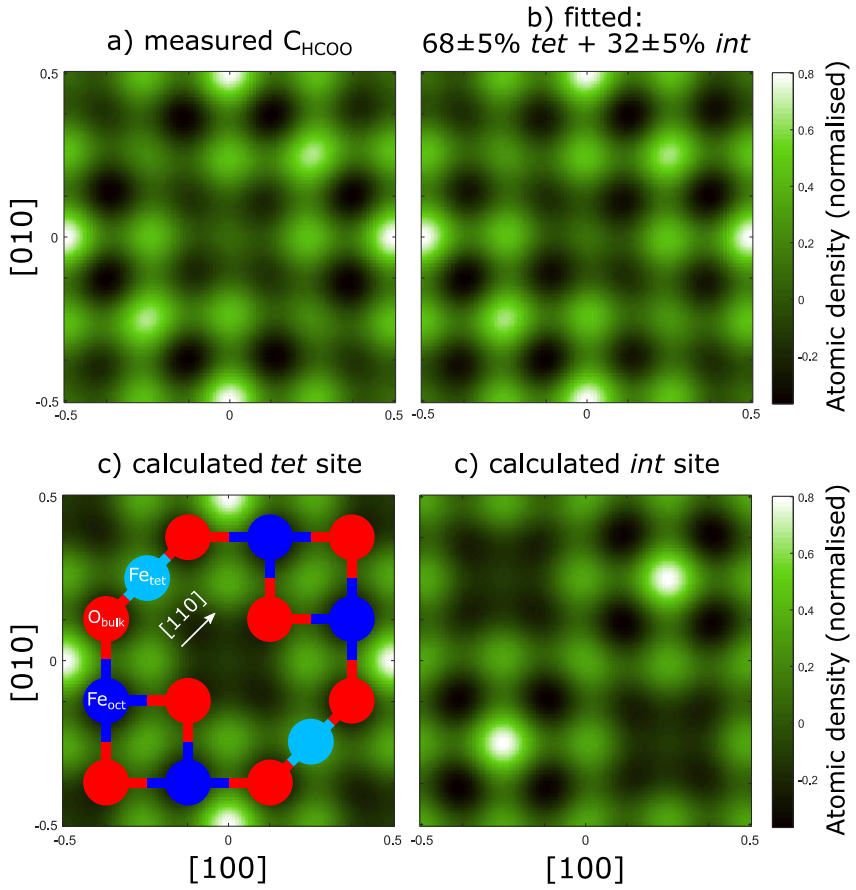

Figure S4 – Given are a) the measured C_{HCOO} real space imaging (as shown in the main article) and b) the fitted real space image comprised of 68 ± 5% C_{HCOO} in the *tet* site and 32 ± 5% C_{HCOO} in the *int* site. Given in c) and d) are the corresponding real space images for the *tet* and *int* site respectively. Note: for the fitting, the complete unit cell of the measured C_{HCOO} density and the calculated *tet* and *int* site densities were used. The images shown here were taken at the corresponding (004) height for the C_{HCOO} species as determined by the NIXSW measurements.

§6 Real space imaging

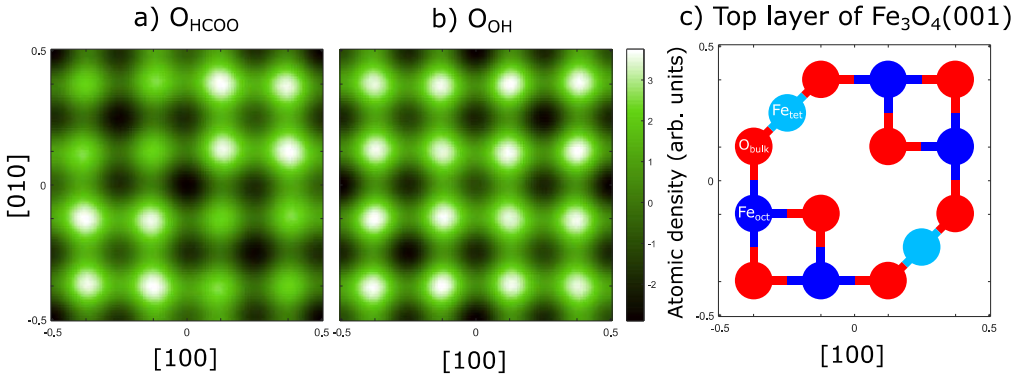

Figure S5 – The real space imaging taken at the corresponding (004) NIXSW heights for the a) O_{HCOO} and b) O_{OH} species. For comparison in c) is given the topmost octahedrally and tetrahedrally coordinated layers of the $Fe_3O_4(001)$ surface.

§7 Other surface terminations - Introduction

In addition to the bulk terminated surface, two other substrate terminations were investigated; an SCV reconstructed surface and a reconstructed surface comprising of no Fe_{tet} interstitial and one subsurface Fe_{oct} cation vacancy (see Figure *S6*) which will be termed the one vacancy structure. With the SCV and one vacancy terminations there are three possible unique sites for the O_{OH} atom: *tet*, int_{α} and int_{β} (see Figure S6). Note that on a bulk terminated surface, the int_{α} and int_{β} site are identical due to the lack of subsurface vacancies and the lack of the interstitial Fe_{tet}. Thus, six different combinations of O_{HCOO} and O_{OH} site were considered.

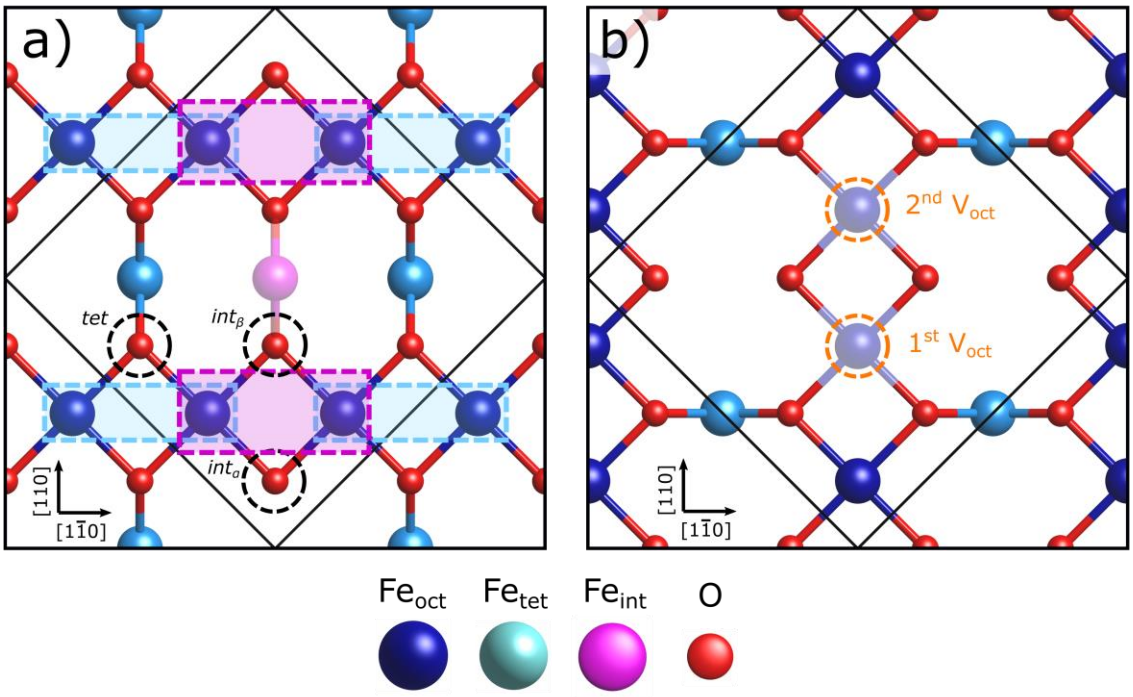

Figure *S*6 - Schematic a is of the topmost octahedral and tetrahedral layers of the $Fe_3O_4(001)$ surface. The light blue boxes mark the surface Fe_{oct} cations that the O_{HCOO} bond to while in the tet site and the larger, purple boxes are for those of the int site. The three O_{OH} sites used in the optimisations (tet, int_{α} and int_{β}) across all substrate structures are marked by the black dotted circles. Note: the O_{OH} int_{α} and int_{β} sites are equivalent for the bulk substrate structure. Schematic b) depicts the next set of octahedral and tetrahedral layers. The orange circles demark the two subsurface cation vacancies of the SCV structure. For the one vacancy structure, only the "1st V_{oct}" is a vacancy.

§8 Other surface terminations – Results

The results of fitting of the PhD data for the SCV and one vacancy structure are provided in Table S2 along with the bulk substrate data from the main article. Out of all four structures optimised, only two other structures fall within the variance of this best fit bulk structure; an SCV and a one vacancy terminated surface both with the formate and O_{OH} atom in equivalent positions to the best fit bulk structure. All structures with the formate in the int position, the O_{OH} at the tet or with the O_{OH} above a subsurface Fe_{oct} cation vacancy, had R-factors higher than the variance of the best fit bulk structure. While there is an SCV and one-vacancy

structure within the variance of the best fit bulk structure, the bulk structure is a better fit to the experimental data and agrees with the results of Arndt et al.[12]

Table S2 - R factors and variances of all 16 optimised structures. The top row structure, a bulk substrate with the formate in the *tet* position and the O_{OH} atom in the *int* position above a subsurface Fe_{oct} cation, is the structure that best fits the experimental PhD modulations with the lowest R factor (= 0.22). Highlighted in bold are the only other structures whose R-factor is within the variance.

Substrate	HCOO position	O_{OH} position	R factor	variance
Bulk	*tet*	*int*	**0.22**	**0.02**
		tet	0.32	0.03
	int	*int*	0.30	0.03
		tet	0.36	0.03
SCV	*tet*	int_{α}	**0.24**	**0.02**
		int_{β}	0.34	0.03
		tet	0.32	0.03
	int	int_{α}	0.26	0.03
		int_{β}	0.34	0.03
		tet	0.34	0.03
One vacancy	*tet*	int_{α}	**0.24**	**0.02**
		int_{β}	0.33	0.03
		tet	0.35	0.03
	int	int_{α}	0.29	0.03
		int_{β}	0.30	0.03
		tet	0.35	0.03

Table S3 gives the optimised vertical relaxation parameters for the first three tetrahedrally and octahedrally coordinated layers of the substrate with all values given as changes from bulk positions as well as the lateral relaxation of the O_{OH} atom in the y direction. The 'bulk' height for the O_{OH} atom is coincident with the surface Fe_{oct} atoms. Note, the larger variance of the parameters for the SCV and one vacancy structures can be attributed to those structures having slightly larger R-factors. The general directions of the relaxations from bulk positions for all three substrate structures are very similar. All substrate layers are found to relax outwards with respect to the idealised bulk-like termination. Generally however, all substrate atoms are found to have moved to more bulklike positions when compared to the LEED-IV determined structure of the SCV reconstruction,[13] corroborating the results of the SXRD study by Arndt et. al.[12] The O_{OH} atom is found to relax inwards towards the Fe_{int} site along the y direction (the crystallographic [110] direction).

Table S3 – Given are the vertical changes from bulk positions for the first three substrate octahedral and tetrahedral layers as well as the lateral y relaxation (in the crystallographic [110] direction) for the O_{OH} atom. Also given are the uncertainties for each parameter.

	Bulk			SCV			One vacancy		
	Δ from bulk (Å)	+	-	**Δ from bulk (Å)**	+	-	**Δ from bulk (Å)**	+	-
O_{OH} - y	0.17	0.2	0.07	0.2	0.2	0.03	0.23		
O_{OH} - z	-0.2	0.1	0.1	0.0	0.2	0.08	0.03		
1st oct layer O - z	0.1	0.2	0.2	0.1	0.2	0.1	0.03		
1st oct layer Fe - z	0.1	0.1	0.1	0.1	0.2	0.07	0.08		
1st tet layer - z	0.5	0.1	0.1	0.1	0.2	0.07	0.08		
2nd oct layer - z	0.1	0.1	0.1	0.1	0.2	0.07	0.15		
2nd tet layer - z	0.2	0.1	0.1	0.2	0.1	0.04	-0.003		
3rd oct layer - z	0.2	n/a	n/a	0.2	n/a	n/a	0.2		
3rd tet layer - z	0.08	n/a	n/a	0.1	n/a	n/a	0.15		

§9 Substrate relaxations

The first three octahedrally coordinated and tetrahedrally coordinated layers of each optimised substrate could relax independently of each other vertically. Only atoms in the top octahedral and tetrahedral layers were allowed to relax in either the x (crystallographic $[1\bar{1}0]$) or y (crystallographic $[110]$) directions, symmetrically about the interstitial site defined as the centre of the unit cell. All surface oxygens not bound to the 1st layer Fe_{tet} atoms were only allowed to relax in the y direction, with positive relaxations being in towards the closest interstitial site. The four oxygens bound to the 1st layer Fe_{tet} atoms and the four surface Fe_{oct} cations were allowed to relax in both the x and y directions, with both the positive y and x relaxations being in towards the central interstitial site. The two Fe cations in the 1st Fe_{tet} layer were relaxed in the x direction only. A schematic showing the positive relaxations of each atom in the top layer is given in the Figure S7. Additionally, five vibrational amplitudes for the Fe_{tet}, Fe_{oct}, O_{bulk}, O_{OH} and O_{HCOO} atoms were optimised as well as the inner potential of the substrate. The additional Fe_{tet} interstitial atom present in the SCV structure was allowed to relax only vertically. In total, 27 parameters for the bulk and one vacancy structures and 28 parameters for the SCV structures were optimised.

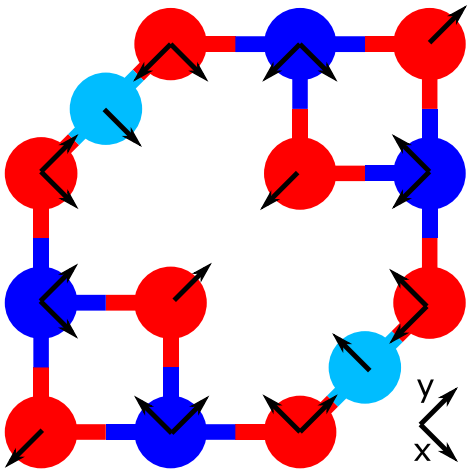

Figure S7 – Shown are the relaxations of the top octahedral and tetrahedral layer atoms in the positive x and y directions. These relaxations were used for all three substrate structures. The additional interstitial Fe_{tet} atom in the SCV structure was only allowed to relax in the vertical direction (out of the plane of the page).

References

1 D. P. Woodruff, Surface structure determination using x-ray standing waves, *Reports Prog. Phys.*, 2005, **68**, 743–798.

2 M. J. Bedzyk and G. Materlik, Two-beam dynamical diffraction solution of the phase problem: A determination with x-ray standing-wave fields, *Phys. Rev. B*, 1985, **32**, 6456–6463.

3 B. W. Batterman, Effect of dynamical diffraction in x-ray fluorescence scattering, *Phys. Rev.*, 1964, **133**, A759–A764.

4 D. P. Woodruff, B. C. C. Cowie and A. R. H. F. Ettema, Surface structure determination using X-ray standing waves: A simple view, *J. Phys. Condens. Matter*, 1994, **6**, 10633–10645.

5 D. P. Woodruff, Adsorbate structure determination using photoelectron diffraction: Methods and applications, *Surf. Sci. Rep.*, 2007, **62**, 1–38.

6 V. Fritzsche, A new spherical-wave approximation for photoelectron diffraction, EXAFS and MEED, *J. Phys. Condens. Matter*, 1990, **2**, 1413–1424.

7 V. Fritzsche, Consequences of a finite energy resolution for photoelectron diffraction spectra, *Surf. Sci.*, 1992, **265**, 187–195.

8 V. Fritzsche, Approximations for photoelectron scattering, *Surf. Sci.*, 1989, **213**, 648–656.

9 R. Dippel, K. U. Weiss, K. M. Schindler, P. Gardner, V. Fritzsche, A. M. Bradshaw, M. C. Asensio, X. M. Hu, D. P. Woodruff and A. R. González-Elipe, A photoelectron diffraction study of the structure of PF3 adsorbed on Ni{in111}, *Chem. Phys. Lett.*, 1992, **199**, 625–630.

10 D. A. Duncan, J. I. J. Choi and D. P. Woodruff, Global search algorithms in surface structure determination using photoelectron diffraction, *Surf. Sci.*, 2012, **606**, 278–284.

11 N. A. Booth, R. Davis, R. Toomes, D. P. Woodruff, C. Hirschmugl, K. M. Schindler, O. Schaff, V. Fernandez, A. Theobald, P. Hofmann, R. Lindsay, T. Gießel, P. Baumgärtel and A. M. Bradshaw, Structure determination of ammonia on Cu(110) - A low-symmetry adsorption site, *Surf. Sci.*, 1997, **387**, 152–159.

12 B. Arndt, K. Sellschopp, M. Creutzburg, E. Grånäs, K. Krausert, V. Vonk, S. Müller, H. Noei, G. B. V. Feldbauer and A. Stierle, Carboxylic acid induced near-surface restructuring of a magnetite surface, *Commun. Chem.*, 2019, **2**, 92.

13 R. Bliem, E. McDermott, P. Ferstl, M. Setvin, O. Gamba, J. Pavelec, M. A. Schneider, M. Schmid, U. Diebold, P. Blaha, L. Hammer and G. S. Parkinson, Subsurface cation vacancy stabilization of the magnetite (001) surface, *Science (80-.).*, 2014, **346**, 1215–1218.